



Cite this: *Nanoscale*, 2015, 7, 8978

## Personalized disease-specific protein corona influences the therapeutic impact of graphene oxide†

Mohammad Javad Hajipour,<sup>a</sup> Jamshid Raheb,<sup>\*a</sup> Omid Akhavan,<sup>d</sup> Sareh Arjmand,<sup>e</sup> Omid Mashinchian,<sup>b,c</sup> Masoud Rahman,<sup>f</sup> Mohammad Abdolahad,<sup>g,h</sup> Vahid Serpooshan,<sup>\*i</sup> Sophie Laurent<sup>j</sup> and Morteza Mahmoudi<sup>\*c,i,k</sup>

The hard corona, the protein shell that is strongly attached to the surface of nano-objects in biological fluids, is recognized as the first layer that interacts with biological objects (e.g., cells and tissues). The decoration of the hard corona (i.e., the type, amount, and conformation of the attached proteins) can define the biological fate of the nanomaterial. Recent developments have revealed that corona decoration strongly depends on the type of disease in human patients from which the plasma is obtained as a protein source for corona formation (referred to as the 'personalized protein corona'). In this study, we demonstrate that graphene oxide (GO) sheets can trigger different biological responses in the presence of coronas obtained from various types of diseases. GO sheets were incubated with plasma from human subjects with different diseases/conditions, including hypofibrinogenemia, blood cancer, thalassemia major, thalassemia minor, rheumatism, favism, hypercholesterolemia, diabetes, and pregnancy. Identical sheets coated with varying protein corona decorations exhibited significantly different cellular toxicity, apoptosis, and uptake, reactive oxygen species production, lipid peroxidation and nitrogen oxide levels. The results of this report will help researchers design efficient and safe, patient-specific nano biomaterials in a disease type-specific manner for clinical and biological applications.

Received 23rd January 2015

Accepted 8th April 2015

DOI: 10.1039/c5nr00520e

www.rsc.org/nanoscale

## 1. Introduction

Graphene is a recently discovered carbon-based nanomaterial that consists of two-dimensional sp<sup>2</sup> hybridized carbon sheets with the thickness of a single atom. Graphene has attracted significant attention as a potential candidate for developing cutting-edge diagnostic (imaging) and therapeutic (e.g., drug delivery, tissue engineering and hyperthermia) approaches.<sup>1–4</sup> Graphene and its derivatives are recognized as the most promising candidates for stem cell-based tissues,<sup>3,5</sup> neural network regeneration<sup>6–8</sup> and cancer diagnosis/therapy due to their excellent physical and chemical properties including their high carrier mobility, mechanical strength and elasticity, surface to volume ratio, and thermal conductivity.<sup>9–16</sup> However, the therapeutic/diagnostic applications of these nanomaterials are hindered because little is currently known about their therapeutic or toxic impacts on the human body.

Currently, it is known that the surfaces of nanomaterials are rapidly covered by different types of biomolecules when they contact biological media.<sup>5,17–20</sup> This shell of biomolecules (the "protein corona") alters the physicochemical properties of the nanomaterials, including their size, charge, roughness, and aggregation state. Thus, the nanomaterials receive a new

<sup>a</sup>Department of Medical Biotechnology, National Institute of Genetic Engineering and Biotechnology (NIGEB), Tehran, Iran. E-mail: jamshid@nigeb.ac.ir

<sup>b</sup>Department of Medical Nanotechnology, School of Advanced Technologies in Medicine (SATiM), Tehran University of Medical Sciences, Tehran, Iran

<sup>c</sup>Nanotechnology Research Center, Faculty of Pharmacy, Tehran University of Medical Sciences, Tehran, Iran

<sup>d</sup>Department of Physics, Sharif University of Technology, P.O. Box 11155-9161, Tehran, Iran

<sup>e</sup>Department of Clinical Biochemistry, Faculty of Medical Science, Tarbiat Modares University, Tehran, Iran

<sup>f</sup>Department of Chemical Engineering and Materials Science, University of California Davis, Davis, CA 95616, USA

<sup>g</sup>Nano Electronic Center of Excellence, Thin Film and Nanoelectronic Lab, School of Electrical and Computer Eng, University of Tehran, P.O. Box 14395/515, Tehran, Iran

<sup>h</sup>Nano Electronic Center of Excellence, Nano Bio Electronic Devices Lab, School of Electrical and Computer Eng, University of Tehran, P.O. Box 14395/515, Tehran, Iran

<sup>i</sup>Cardiovascular Institute, Stanford University School of Medicine, Stanford, California, USA. E-mail: vserp1@stanford.edu, Mahmoudi@stanford.edu

<sup>j</sup>Department of General, Organic and Biomedical Chemistry, NMR and Molecular Imaging Laboratory, University of Mons, 19 Avenue Maistriau, B-7000 Mons, Belgium

<sup>k</sup>Division of Cardiovascular Medicine, Department of Medicine, Stanford University School of Medicine, Stanford, California, USA

†Electronic supplementary information (ESI) available. See DOI: 10.1039/c5nr00520e

biological identity that may be entirely different from their original pristine identity.<sup>17,21,22</sup> Therefore, biological entities (*e.g.*, organs, tissues, and cells) “see” this newly obtained identity when interacting with the nano biomaterials.<sup>23</sup>

Previously, it was shown that the protein composition of the corona determines the therapeutic/toxic effects of the nanomaterials and the physiological response of the host body.<sup>21,24–26</sup> Recently, we showed that the protein composition/content of corona coating at the surface of superparamagnetic zinc ferrite spinel-graphene nanostructures significantly affect their therapeutic/toxic impacts against breast cancer cells.<sup>27</sup>

The protein composition and content in the corona depend on several parameters, including the personalized plasma alterations that result in a personalized protein corona,<sup>28</sup> incubation time and temperature,<sup>29–31</sup> protein/nanomaterial surface area ratio,<sup>32</sup> protein gradient concentration,<sup>33</sup> local temperature at the nanomaterial surface,<sup>34</sup> protein source,<sup>35</sup> and the physicochemical properties of the nanomaterial (*e.g.*, size, shape, charge, and composition).<sup>18,32,36–39</sup> Tenzer *et al.*<sup>31</sup> demonstrated that the corona content was quantitatively altered during different exposure times (0.5–480 min). However, the corona composition did not change. Due to the protein content variations in the corona layer, the hard coronas that were obtained at various exposure times exhibited different pathophysiological effects. Recently, we showed that the plasma alterations mediated by different disease/situations/lifestyles affect the protein composition and contents of the corona.<sup>28</sup> Our results indicated that identical nanoparticles have different corona protein compositions/contents when administered in human patients because individuals exhibit distinct (personalized) plasma alterations depending on their health conditions, lifestyle, and genetic background. Recently, Caracciolo *et al.*<sup>40</sup> also approved the personalized protein corona formation in individual patients by incubating lipid NPs with the plasmas of healthy and pancreatic cancer patients. They showed that the corona-coated lipid NPs from healthy and pancreatic cancer patients had a different size and surface charge which is in close agreement with our study.

Due to their inter-individual heterogeneity, patients display different susceptibilities and therapeutic responses to the same drugs. Therefore, to improve personalized nanomedicine and achieve maximal therapeutic efficacy with minimal side effects, it is necessary to track the therapeutic or toxic effects of nanomaterials in different individuals. Although multiple reports have discussed the biological effects of graphene and its derivatives,<sup>41,42</sup> the therapeutic and toxic impacts of these nanomaterials in different patients have not been investigated. Herein, we evaluate the interactions between corona-coated graphene oxide (CCGO) sheets and two different cell types (MCF-7 and MDA-MB-231). The GO sheets were incubated with the human plasma from subjects with different diseases/conditions, including hypofibrinogenemia, blood cancer, thalassemia major, thalassemia minor, rheumatism, favism, hypercholesterolemia, diabetes, and pregnancy. To the best of our knowledge, this is the first study that has tracked the

therapeutic/toxic impacts of CCGO sheets on different patients.

## 2. Materials and methods

### 2.1. Synthesis of the GO suspension

Natural graphite powder (Fluka, particle diameter of  $\leq 20 \mu\text{m}$ ) was used as the raw material to produce the graphite oxide suspensions according to the modified Hummers' method (details can be found in ref. 43). The synthesized graphite oxide powder was dispersed in deionized (DI) water, which yielded an aqueous suspension with a yellow-brownish color. To remove the unexfoliated graphitic plates and the tiny graphite particles, the obtained aqueous suspensions were centrifuged at 2000g and 12 000g for 30 min, respectively. Finally, the well-dispersed colloidal GO sheets were obtained by exfoliating the filtered graphite oxide suspension by using sonication at a frequency of 40 kHz with a power of 150 W for 30 min.

### 2.2. Material characterization

The surface topography and height profiles of the GO sheets were examined using atomic force microscopy (AFM, Digital Instruments NanoScope V) in the tapping mode. X-ray photoelectron spectroscopy (XPS) was used to investigate the chemical states of the GO sheets. The data were gathered using a hemispherical analyzer that was supplied with an Al K $\alpha$  X-ray source ( $h\nu = 1486.6 \text{ eV}$ ) operating under vacuum of more than  $10^{-7} \text{ Pa}$ . The XPS peaks were deconvoluted by using Gaussian components after a Shirley background subtraction. The carbon structures of the GO sheets were studied by using Raman spectroscopy (HR-800 Jobin-Yvon) at room temperature with an Nd-YAG laser source operating at a wavelength of 532 nm. For the AFM, XPS, and Raman spectroscopy, each sample was prepared by drop-casting the desired graphene-containing suspension onto a cleaned SiO<sub>2</sub>/Si(100) substrate before drying at 110 °C in a vacuum (with a pressure of  $\sim 0.8 \text{ Pa}$ ) for 30 min. To improve the AFM imaging, a diluted GO suspension (0.01 mg mL<sup>-1</sup>) was utilized.

### 2.3. Sample preparation

The blood samples were collected from volunteer patients (patients with specific disease types) according to ethical and medical law at the Persian Gulf hospital. Age and sex-matched patients (except for pregnant cases) were selected for this study. For this purpose, personal consultations were conducted between physicians and patients after informed consent was obtained from the subjects. Each blood sample was collected in commercially available citrated tubes and centrifuged at 2500g for 5 min at 4 °C. Finally, the supernatants were collected, divided, and stored at -70 °C. In some cases, the blood samples were centrifuged twice to eliminate all of the blood cells.<sup>28</sup>

## 2.4. Protein corona preparation

The hard corona-GO complex was obtained by following a well-established protocol.<sup>44</sup> Because slight temperature changes can affect the formation of the protein corona,<sup>29,34</sup> the GO sheets and plasmas were pre-incubated at 37 °C for 5–10 min. Next, 900  $\mu\text{L}$  of the diluted plasmas (5% and 50%) from the different patients were incubated with 100  $\mu\text{L}$  of the graphene oxide sheets (with a concentration of 1  $\text{mg mL}^{-1}$ ) at 37 °C for 1 h. In the next step, each reaction mixture was centrifuged for 30 min at 18 000g (temperature of 15 °C) to obtain a pellet of the protein corona-GO complexes. Then, the pellets were re-suspended in 1 mL of PBS (15 °C) before centrifuging for 20 min at 18 000g and 15 °C (washing step). This washing step was repeated three times to remove the excess and loosely attached proteins on the surfaces of the sheets. The final pellet was re-suspended in PBS and used for the subsequent analyses.

## 2.5. SDS-PAGE and ImageJ analyses

The obtained hard corona-GO complexes were re-suspended in a protein loading buffer and boiled for 10 min at 100 °C. The same volume of each sample was loaded into 15% polyacrylamide gel before running at 120 V and 80 mA for approximately 100 min. The gels were stained using the silver nitrate protocol. A semi-quantitative densitometry measurement was used to determine the intensities of the protein bands that were involved in the hard coronas of the various patients. In this regard, the ImageJ software (Version 1.410) was used to measure the quantities of the protein bands across three different ranges (>100 kDa, 100–40 kDa and <40 kDa).

## 2.6. Dynamic light scattering (DLS) and zeta potential

The DLS and zeta potential of the CCGO sheets from all of the patients were measured using a Malvern PCS-4700 instrument that was equipped with a 256-channel correlator and Malvern zeta sizer 3000 HSA, respectively. These analyses were performed by averaging six replicates of each sample (100  $\mu\text{g mL}^{-1}$ ) at 25 °C.

## 2.7. Cell culture and treatment

The MCF-7 and MDA-MB-231 cells (breast cancer cells) were obtained from the National Cell Bank of Iran (NCBI) at the Pasteur Institute of Iran. The cells were seeded in 96-well plates at a concentration of  $\sim 10\,000$  cells per well with 100  $\mu\text{L}$  of the medium for 24 h at 37 °C in a 5%  $\text{CO}_2$  incubator. These cells were cultured in a pyruvate-free DMEM culture medium that was supplemented with 10% heat inactivated fetal bovine serum and antibiotics (100  $\mu\text{g mL}^{-1}$  streptomycin and 100 U  $\text{mL}^{-1}$  penicillin). After 24 h (with 70% cell confluency), the medium was replaced with 150  $\mu\text{L}$  of the fresh FBS-free medium that contained the CCGO sheets (100  $\mu\text{g mL}^{-1}$ ) and was incubated for 4–24 h. Fresh FBS-free media without any CCGO sheets were used for the control cells. All materials were purchased from Gibco-USA.

## 2.8. MTT assay

The cytotoxicity was quantitatively measured using the (3-(4,5-dimethylthiazol-2-yl)-2,5-diphenyltetrazolium bromide) MTT assay (Sigma-Aldrich). At two time points after incubating the cells with the CCGO sheets (4 and 24 h), each well was washed with PBS and 100  $\mu\text{L}$  of the MTT solution (0.5  $\text{mg mL}^{-1}$ ) was added to each of the wells in the 96-well plates. Following 3 h of incubation, the medium was replaced with 100  $\mu\text{L}$  of dimethyl sulfoxide (DMSO) to solubilize the formazan crystals. The absorbance of each well medium was measured on a micro plate reader (Labsystem multiskan MS) at 570 nm.

## 2.9. Reactive oxygen species (ROS) assay

At two time points following incubation of the cells with the CCGO sheets (4 and 24 h), the cells were rinsed with PBS (two times) and incubated with 5-(and-6)-chloromethyl-2,7-dichloro-dihydrofluorescein diacetate acetyl ester (H2 DCFDA), with a final concentration of 10 mM for 60 min at 37 °C. Then, the cells were washed with PBS and the fluorescence intensities of the media in each well were measured using a spectrofluorometer (excitation: 480 nm; emission: 435 nm). The results were expressed as the relative fluorescence intensity for each sample.

## 2.10. Lipid peroxidation assay

The degree of membrane lipid peroxidation (LPO) was determined using spectrophotometrical measurements of the MDA as an end product of the LPO process.<sup>45</sup> In this case, 1 mL of the trichloroacetic acid (TCA) solution (5%, wt/vol) was added to 1 mL of the cell mixture (0.1 mL of cell and 0.9 mL of PBS (pH 7.4)). After precipitation, the final mixture was centrifuged at 3800g for 10 min. Subsequently, 1 mL of thiobarbituric (1%) was added to the supernatant and boiled for 15 min at 100 °C. Finally, the mixture was cooled to room temperature and the absorbances of each mixture were read at 523 nm (Labsystem multiskan MS).

## 2.11. Nitric oxide level measurements

The extent of the produced  $\text{NO}_2^-$  was measured using the spectrophotometrically based Griess test, which assesses the  $\text{NO}_2^-$  levels that are released into the cell culture media.<sup>46</sup> After incubating the cells with the corona coated GO sheets, 100  $\mu\text{L}$  of the supernatant (cell culture media) were added to the cryovials containing an equal volume of the Griess reagents (1% sulfanilamide, 1% naphthylethylene diamine dihydrochloride and 2%  $\text{H}_3\text{PO}_4$ ) and incubated at 25 °C for 15 min. The absorbance of each well medium was measured at 550 nm using a Micro plate reader (Labsystem multiskan MS).

## 2.12. Determination of the protein carbonyl content (PCO)

The level of protein oxidation was assessed by measuring the amount of carbonyl formation, which is known as the index of PCO, by using a spectrophotometric assay. The PCOs were assessed by using the approach of Reznick and Packer.<sup>47</sup> Briefly, the supernatant was transferred into two tubes before

1 mL of 20 mM DNPH dissolved in 2 M HCl was added to one of the tubes and 1 mL of 2 M HCl was added to the other tube. The tubes were stored for 1 h at room temperature. In the next step, the proteins were precipitated by adding 2 mL of trichloroacetic acid (20% wt/vol) to each tube and the tubes were maintained on ice for 15 min. After centrifugation at 4800g for 15 min, the supernatant solutions were removed and the pellets were rinsed three times with ethanol/ethyl acetate (1 : 1 vol/vol). Finally, the precipitates were dissolved in 1 mL of the guanidine hydrochloride solution before measuring the absorbance of each sample at 370 nm using a Micro plate reader (Labsystem multiskan MS).

### 2.13. Double staining for necrosis and apoptosis using annexin V and propidium iodide (PI)

The double staining assay of the cell-CCGO sheets that exhibited cross-talk was performed using the Annexin-V-Fluorescein kit (Roche) according to the manufacturer's instructions. The cells were incubated with different CCGO sheets for 24 h and then washed with PBS. To stain  $2 \times 10^6$  cells, the staining solution (containing 40  $\mu$ l of the Annexin-V-Fluorescein labeling reagent diluted in 2000  $\mu$ l HEPES buffer and 40  $\mu$ l propidium iodide) was added to the wells before incubating for 15 min at room temperature in the dark. Finally, the cells were washed, mounted on the microscope slides (Zeiss (axiaphot)), and the early apoptotic cells (Annexin V+ only (green)) and late apoptotic/necrotic cells (Annexin V+ and PI+ (yellow/red)) were counted.

### 2.14. Lysosome labeling

After incubating the MCF-7 and MDA-MB-231 cells with different CCGO sheets at a final concentration of 100  $\mu$ g ml<sup>-1</sup>, the media were discarded and the cells were washed with PBS solution. In the next step, the cells were labeled with Lyso-tracker® Red DND 99 dye to stain the lysosomes (Image-iT™ LIVE lysosomal and nuclear labeling kit) according to the manufacturer's instructions. Briefly, the cells were incubated for 1 h with the 10 nM Lyso-tracker® Red DND 99 dye, washed with PBS and incubated with acridine orange dye (1  $\mu$ M) for 10 min. Finally, the cells were rinsed three times before being visualized on confocal microscope slides (Leica, TCS SP5).

### 2.15. Circular dichroism (CD) spectroscopy

The CD analysis was conducted to identify the conformational changes of the fibrinogen and bovine serum albumin (BSA) proteins under different GO concentrations. The purchased fibrinogen (sigma) and/or BSA proteins (sigma) were dissolved in the PBS buffer solution (250  $\mu$ g ml<sup>-1</sup>) and incubated with different GO concentrations of 10 to 400  $\mu$ g ml<sup>-1</sup> for 1 h at 37 °C. All of the CD measurements were performed between wavelengths of 190 and 260 nm with an average of 3 scans by using a spectropolarimeter (Jasco-J 715). The results were shown as residual ellipticity (MRE) in deg.

### 2.16. Hemolysis assay

Blood was taken from a volunteer who had no blood disorder, collected in heparinized tubes and centrifuged at 500g for 5 minutes. The cell pellet was suspended in PBS and centrifuged at 500g for 5 minutes (washing step). The washing step was repeated five times and then the washed red blood cells (RBCs) were diluted in PBS. The CCGO sheets at a final concentration of 500  $\mu$ g ml<sup>-1</sup> were added to RBC stock solutions containing approximately  $4.5 \times 10^8$  erythrocytes and incubated at 37 °C for 180 minutes. Finally the samples were centrifuged at 2500g for 5 minutes and the level of hemoglobin release in the supernatant was determined at 540 nm using a microplate reader (Labsystem multiskan MS). In this assay, the mixture solutions of RBCs with PBS containing 10% Triton X-100 and RBCs with PBS alone were used as positive and negative controls respectively. Percentage of hemolysis was estimated according to the typical formula.

### 2.17. Statistical analysis

All experiments were replicated three times and the standard deviation is showed with error bars. A comparison of different groups was performed using SPSS software to determine differences ( $P < 0.05$ ).

## 3. Results and discussion

### 3.1. Synthesis and characterization of graphene oxide sheets

Graphene oxide (GO) sheets were deposited on a SiO<sub>2</sub>/Si substrate and were characterized using atomic force microscopy (AFM) (Fig. 1A). Overlapped GO sheets are distinguishable in the AFM image. In addition, the height profile distributions of the sheets are given in Fig. 1B. The typical thickness of the monolayered GO sheets is ~0.8 nm (~0.44 nm thicker than graphene, with a thickness of ~0.36 nm) due to the presence of oxygen groups that bond to the GO surface.<sup>48–50</sup> The first peak in the height profile distributions indicated surface roughness fluctuations, and the second peak at ~0.8 nm indicated the presence of monolayered GO sheets on the substrate. The appearance of a relatively weak peak at ~1.8 nm indicated that bilayered and multi-layered GO sheets were not abundant (Fig. 1B).

The deconvolution of the C(1s) core-level X-ray photoelectron spectroscopy (XPS) peak was performed to investigate the chemical state of the GO sheets (Fig. 1C). From the peak deconvolution, the peak centered at 285.0 eV was attributed to the C–C and C=C bonds. Additional deconvoluted peaks were located at binding energies of 286.6, 287.3, 288.2 and 289.3 eV and were attributed to the C–OH, C–O–C, C=O, and O=C–OH oxygen-containing functional groups, respectively.<sup>51,52</sup> The O/C atomic ratio was evaluated to be equal to approximately 0.48.

Raman spectroscopy was used to investigate the carbon structure of the GO sheets. The two well-known Raman bands of carbon materials include the G (~1575 cm<sup>-1</sup>) and the D (~1345 cm<sup>-1</sup>) bands (Fig. 1D). The G band results from the E<sub>2g</sub> phonon that is scattered from the graphitic structure. The D

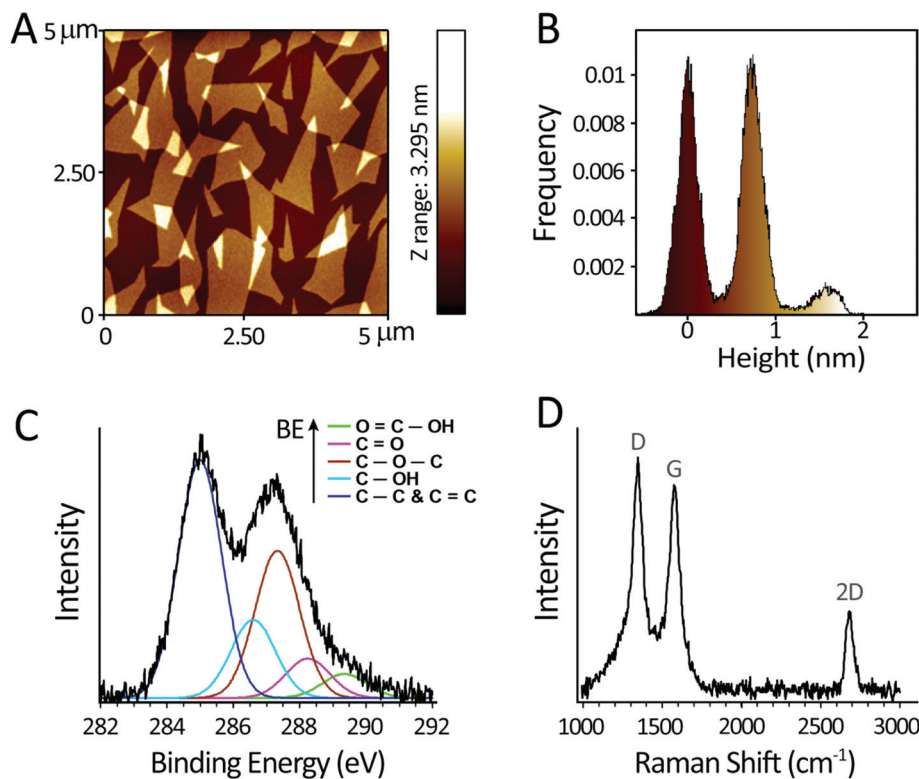


Fig. 1 (A) AFM image of synthesized GO and (B) height profile distribution of the sheets shown in (A); (C) peak deconvolution of the C (1s) core level of the XPS spectrum and (D) Raman spectrum of the as-prepared GO.

band is assigned to the  $sp^3$  defect bonds of the breathing mode of the  $k$ -point phonons with a  $A_{1g}$  symmetry.<sup>53,54</sup> In addition, the D band can originate from vacancies, grain boundaries, edge defects and amorphous carbon species in a disordered carbon structures.<sup>55</sup> The 2D band in the Raman spectra of the graphene materials is sensitive to stacking of the sheets.<sup>56</sup> For example, the 2D band of the monolayered graphene occurs at  $\sim 2679\text{ cm}^{-1}$ . In contrast, the 2D band for multi-layered graphene (containing 2–4 layers) appears as a broadened peak with a  $19\text{ cm}^{-1}$  shift towards greater wavelengths.<sup>57</sup> Furthermore, the  $I_{2D}/I_G$  intensity ratios of mono-, bi-, triple- and multi- (>4) layered graphene are  $>1.6$ ,  $\sim 0.8$ ,  $\sim 0.30$  and  $\sim 0.07$ , respectively.<sup>58–60</sup> In this study, the  $I_{2D}/I_G$  ratio of the GO sheets was 0.42, which corresponded to the presence of <3-layered sheets and was consistent with the results obtained by the AFM analysis.

### 3.2. The effects of plasma alterations mediated by different diseases on the GO-corona composition (personalized protein corona)

To study the effects of plasma alterations related to different diseases on the GO-corona composition, monolayered GO sheets were incubated with the plasmas that were collected from volunteers with different types of diseases/conditions, including healthy, pregnancy, favism, rheumatism, diabetes, hypercholesterolemia, thalassemia minor, thalassemia major,

blood cancer, and hypofibrinogenemia conditions. Next, the excess plasma and loosely attached proteins ('soft corona') were removed. The resulting corona-coated graphene oxide (CCGO) sheets consisted of tightly bound proteins that did not detach during multiple centrifugation and washing steps. The protein patterns of the different coronas that were obtained by gel electrophoresis indicated significant variations in the compositions of the hard corona of the different patients (Fig. 2A). Furthermore, a number of protein bands (marked by yellow arrows) appeared/disappeared in the hard coronas from a fraction of the patients, while the rest of the bands were present in the coronas from all of the patients. Several diseases, including blood cancer, hypofibrinogenemia, diabetes, and hypercholesterolemia, yielded distinctly different corona compositions relative to the other diseases.

The results obtained in this study agree with our recent findings, implying that identical nanoparticles may attain different corona protein compositions/contents in various patients.<sup>28</sup> The variations of the hard corona profile in the plasmas from patients with different diseases can be attributed to alterations in the plasma protein compositions/content, the protein conformation, and/or the protein solubility under different disease conditions. Predetermined plasma protein variations could affect the adsorption affinity of proteins with the surface of nanomaterials. Previously, protein corona studies overlooked possible protein composition/content

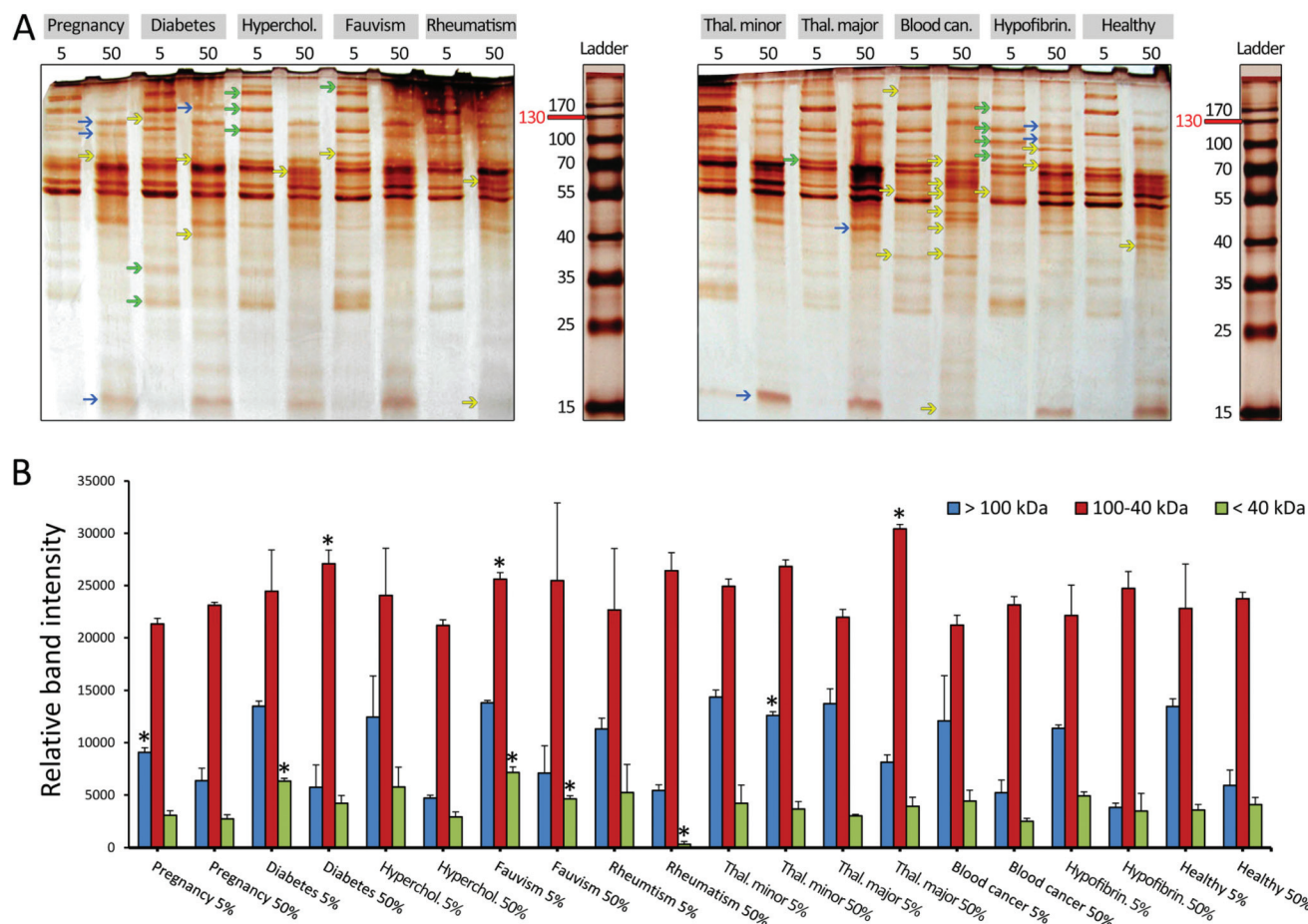


**Fig. 2** (A) SDS-PAGE gel (15%) of CCGO obtained following incubation with 5% and 50% plasmas of different patients (pregnancy, diabetes, hypercholesterolemia, fauvisim and rheumatism, thalassemia minor/major, blood cancer, hypofibrinogenemia and healthy). The green and blue arrows mark the proteins that only appeared in the hard corona of 5% and 50% plasmas respectively. The yellow arrows mark the protein bands that specifically appeared/disappeared in the hard corona of a fraction of patients. (B) Relative amount of the proteins associated within the CCGO after incubation with 5% and 50% plasmas of different patients (pregnancy, diabetes, hypercholesterolemia, fauvisim, rheumatism, thalassemia minor/major, blood cancer, hypofibrinogenemia and healthy). The relative protein intensity of CCGO from plasmas with a similar concentration was compared to each other. The significant differences among total band intensities of proteins (categories) with similar molecular weights were calculated using SPSS software. Star (\*) represents significant differences ( $P < 0.05$ ) compared to other patients.

variations in different patients. Thus, a number of researchers have documented contradictory results.<sup>31</sup> Here, we observed that protein corona formation is a multi-factorial process that can be affected by different stimuli that influence the plasma protein hemostasis. In agreement with this finding, Tenzer and coworkers<sup>31</sup> confirmed that the formation of the protein corona cannot be described by only the Vroman effect.

In addition to the specific protein concentration variations in the plasma, the protein/nanomaterial surface area ratio (*i.e.*, incubation of various plasma concentrations with the exact same nanomaterial concentrations) can also play a critical role in the concentrations and compositions of the bound proteins.<sup>32</sup> To investigate the effects of the various plasma concentrations (*i.e.*, protein/GO sheets surface area ratio), the sheets were incubated in two plasma concentrations (5 and 50%) for each patient and the resulting CCGO sheets were evaluated using 1D-SDS-PAGE. Based on the protein patterns of the hard

coronas (Fig. 2A), evident differences were observed between the compositions of the coronas that were formed in 5% and 50% plasma. The protein bands marked by green and blue arrows in Fig. 2A only appeared/disappeared in the hard corona formed in 5% and 50% plasma, respectively. Some protein bands with molecular weights between 70 and 100 kDa steadily appeared in the hard coronas of both plasma concentrations (5 and 50%). Based on these results, it was suggested that the single layered GO sheets have different potential affinities for plasma proteins when they are incubated in plasmas with different concentrations.

To compare the obtained protein patterns of the various CCGOs quantitatively, the relative intensities of the proteins bound to the GO sheets were measured using the ImageJ software (version 1.410). Because most of the hard corona consists of proteins with molecular weights of 40 to 100 kDa, the protein bands were classified based on the following three

**Table 1** DLS and zeta potential data from CCGO obtained after incubation with 5% and 50% plasmas of different patients

Disease/situation	DLS-plasma 5% (nm)	Zeta-plasma 5% (mV)	DLS-plasma 50% (nm)	Zeta-plasma 50% (mV)
Healthy	1466 ± 170	-5.93	1398 ± 231	-7.33
Pregnancy	1329 ± 245	-8.31	1293 ± 266	-9.37
Diabetes	1236 ± 231	-7.32	1209 ± 180	-8.42
Hypercholesterolemia	1304 ± 237	-7.46	1362 ± 241	-7.76
Rheumatism	1378 ± 211	-7.08	1407 ± 219	-8.27
Thalassemia minor	1228 ± 242	-7.93	1298 ± 299	-9.21
Thalassemia major	1272 ± 253	-8.03	1232 ± 244	-8.49
Fauvism	1130 ± 253	-7.01	1196 ± 283	-8.84
Blood cancer	1298 ± 246	-7.00	1226 ± 222	-9.25
Hypofibrinogenemia	1228 ± 229	-6.71	1263 ± 278	-7.79

**Table 2** DLS and zeta potential data from bare GO

Nanoparticle	DLS (nm)	Zeta potential (mV)
Graphene oxide	1169 ± 212	-18.8

molecular weight categories: <40, 40–100, and >100 kDa. The relative densitometry results showed that the intensities of the proteins bound to the GO sheets were different for different patients and plasma concentrations (Fig. 2B). This result agrees with the previous observations of silica and polystyrene NPs indicating that the protein content of corona changed for different patients.<sup>32,33</sup> These differences are potentially related to the plasma protein variations and the ratio between the plasma protein concentration and the total GO surface area.

In addition to the gel electrophoresis analysis, dynamic light scattering (DLS) and zeta potential analyses were employed to measure the size distributions and zeta potentials of the CCGO sheets from different patients and with varying protein/GO surface area ratios. Furthermore, DLS and zeta potential analyses revealed that the size and surface charge of the CCGO sheets from various patients and plasma concentration were different (see Tables 1 and 2 for details). We also performed AFM to track the thickness of protein corona in selected diseases and revealed that corona thickness is dependent on the type of disease (Fig. S1 and S2 of ESI†).

### 3.3. Cellular responses to the GO sheets coated with the hard corona from various diseases

Slight changes in the decoration of the protein corona (type, amount, or conformation of associated proteins) can significantly alter the cellular response to nanomaterials.<sup>61,62</sup> Therefore, the protein coronas obtained from various diseases may induce different cellular responses to nanomaterials. We investigated the cellular morphology (Fig. S3 and S4 of ESI†), cellular toxicity, production of reactive oxygen species (ROS), oxidative stress (MDA and PCO), inflammation, apoptosis/

necrosis and cellular uptake in the presence of CCGO sheets that were obtained from different patients.

**3.3.1. Cellular toxicity of the hard corona-coated GO sheets.** In this study, CCGO sheets were incubated with breast cancer cell lines (MCF-7 and MDA-MB-231) and their cytotoxicity was probed using the MTT viability assay. The CCGO sheets from various patients and different protein/sheet surface ratios (5% and 50%) exhibited similar toxicities against MDA-MB-231 cells; in the same way, the coated sheets exhibited approximately the same toxicity to the MCF-7 cells, except for the CCGO sheets that were obtained from the blood cancer patients (see Fig. 3A–D). For the majority of the tested diseases, the protein corona formed on the GO sheets did not considerably increase the cell cytotoxicity. Thus, the formation of a protein corona may reduce the cytotoxicity of GO sheets by preventing physical damage to the cell membrane (as reported by Hu *et al.*).<sup>42</sup>

The only significantly different (higher) toxicity result was obtained for the CCGO sheets that were incubated in the plasma from the blood cancer patients (50%). As shown in Fig. 2A, the resulting protein corona patterns were different in this plasma relative to the other plasmas, which suggested that a greater cytotoxicity effect of the CCGO sheets may be related to their corona components. In contrast, the sheets that were obtained from different plasma concentrations (5% and 50%) had similar cytotoxicities against the breast cancer cells.

**3.3.2. The generation of ROS by the CCGO sheets.** Although normal ROS concentrations play an important role in different cellular processes, such as cell proliferation and signal transduction, excessive ROS concentrations result in cell apoptosis and necrosis that can be beneficial in cancer therapy applications.<sup>63</sup> Therefore, increasing and decreasing the ROS concentrations can serve as promising strategies for destroying cancer cells.<sup>64,65</sup> The CCGO sheets from various patients were incubated with breast cancer cells to evaluate the effects of personalized coronas on the ROS production. Sheets with different coronas produced different amounts of ROS after 24 h of incubation. For the MCF-7 cells, the CCGO sheets from the thalassemia major (5% and 50%), pregnancy (5%), diabetes (5%) and rheumatism (50%) patients produced the highest ROS levels relative to the other patients (Fig. 4A and B). For the MDA-MB-231 cells, the CCGO sheets from the hypercholesterol (5% and 50%), blood cancer (5% and 50%) and fauvism (5% and 50%) patients resulted in the highest ROS levels (Fig. 4C and D). This finding suggests that cancer cells may have different resistance/susceptibility to sheets that are obtained from various patients.

The mechanisms by which the CCGO sheets exert oxidative stress remain elusive. Nanomaterials can increase the intracellular ROS levels through physical interactions with the plasma membrane, by internalization into the cells (and subsequent interaction with the mitochondria, reticulum endothelial system, and hydrogen peroxide), and by perturbing the antioxidative defense system.<sup>66–68</sup> Thus, the CCGO sheets from the plasma of various patients may interact differently with the

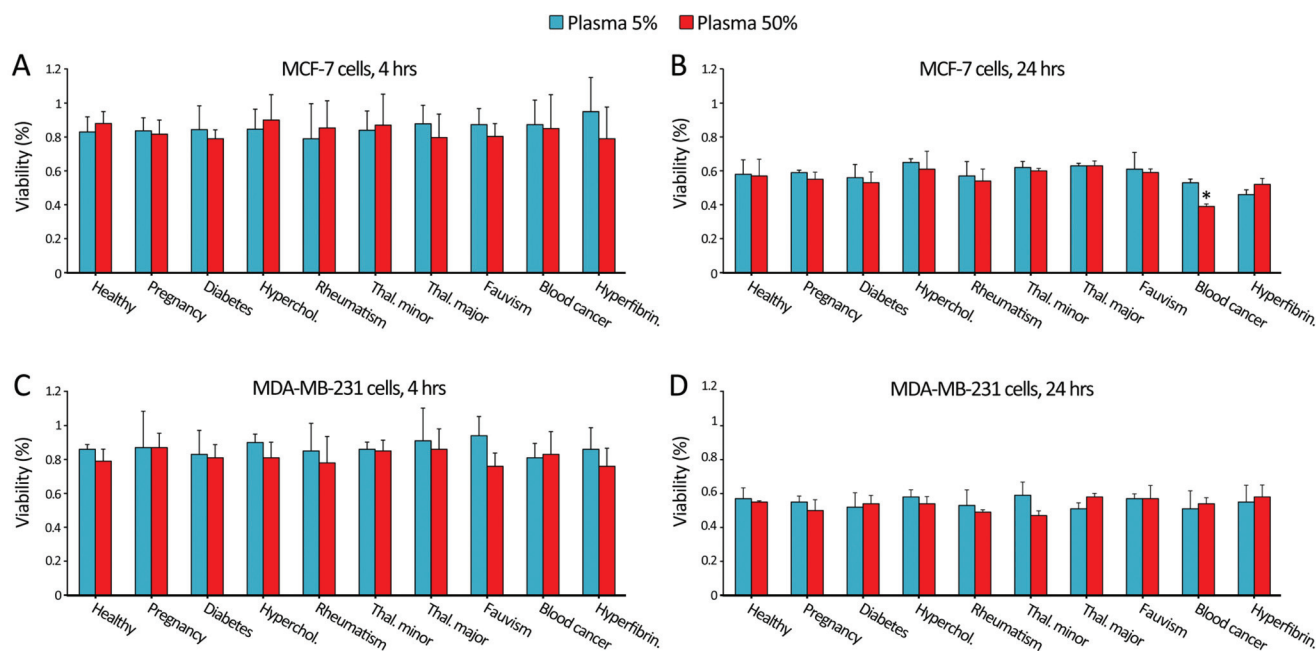


**Fig. 3** Cell viability of (A and B) MCF-7 and (C and D) MDA-MB-231 cells incubated with CCGO ( $100 \mu\text{g ml}^{-1}$ ) from different patients for (A and C) 4 hours and (B and D) 24 hours. The cytotoxicity of CCGO from plasmas with a similar concentration was compared to each other. Star (\*) represents significant differences ( $P < 0.05$ ) compared to other patients.

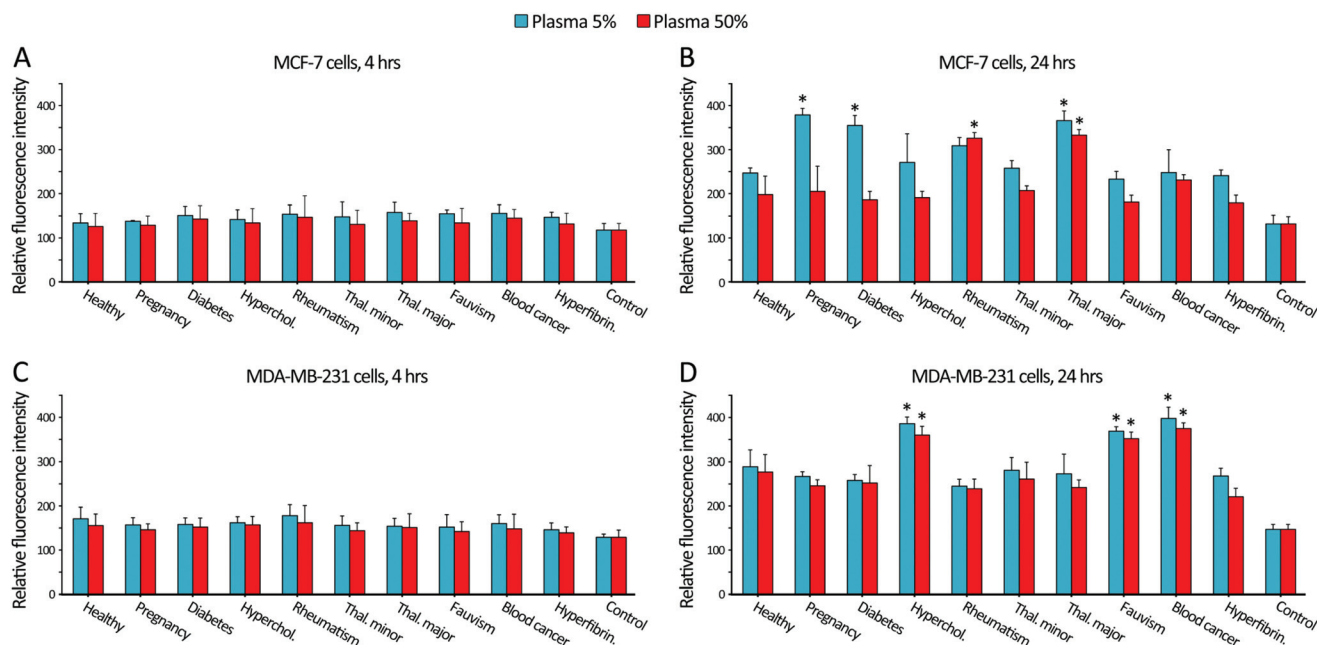


**Fig. 4** Level of ROS production in (A and B) MCF-7 and (C and D) MDA-MB-231 cells incubated with CCGO ( $100 \mu\text{g ml}^{-1}$ ) from different patients for (A and C) 4 hours and (B and D) 24 hours. The ROS production induced by CCGO from plasmas with a similar concentration was compared to each other. Star (\*) represents significant differences ( $P < 0.05$ ) compared to other patients.

cancer cells and induce different oxidative stress components/levels. In addition, variations in the ROS production may be attributed to the different cellular uptake capacities of the CCGO sheets.

**3.3.3. Oxidative stress and inflammation responses induced by the CCGO sheets.** Oxidative stress can affect cells depending on the type, level, and location of the generated ROS and on the period of oxidant production and the cell type.

ROS can oxidize critical biomolecules, such as proteins, lipids and DNA, which often results in the loss of their function.<sup>69</sup> Protein carbonylation is an oxidative stress impairment that can be caused by different oxidative pathways.

In this study, the CCGO sheets were incubated with the cells and the extent of protein carbonylation was measured as an index of protein oxidation, which reflected the downstream cellular damage caused by the ROS. The protein carbonylation levels were approximately identical for all of the CCGO sheets (Fig. 5A and B), suggesting that the corona components had negligible contributions to protein carbonylation. The oxidative change in polyunsaturated fatty acids, is one primary consequence of elevated oxidative stress. Lipid peroxidation results in the production of malondialdehyde (MDA) as an index of lipid peroxidation and indirectly reflects the degree of cell damage.<sup>70</sup> We measured the MDA level after incubating the CCGO sheets from the patients with MCF-7 and MDA-MB-231 cells. The sheets that were obtained from rheumatism (5% and 55%) and hypofibrinogenemia (5%) induced

significantly greater MDA levels in the MCF-7 cells than those of the other patients (Fig. 5C). In the MDA-MB-231 cell, the CCGO sheets from thalassemia minor (5% and 50%) and pregnancy (50%) generated the highest amounts of MDA (Fig. 5D). The different levels of lipid peroxidation potentially resulted from the generation of different species and amounts of ROS and from the generation of different oxidative stress by-products from the various CCGO sheets. In contrast, the cells may respond differently to the CCGO sheets that were obtained from various patients.

Cellular inflammation can induce the formation of chemical intermediates, such as nitric oxide (NO), that damage biomolecules. In addition, NO induces genotoxicity and affects the angiogenesis and metastasis of tumor cells.<sup>71</sup> We measured the NO concentration as an index of cellular inflammation after incubating the CCGO sheets of various patients with cancer cells (Fig. 5E and F). The MDA-MB-231 cells exhibited the greatest inflammation response (NO level) to the CCGO sheets from the thalassemia major (5%) and hypofibri-

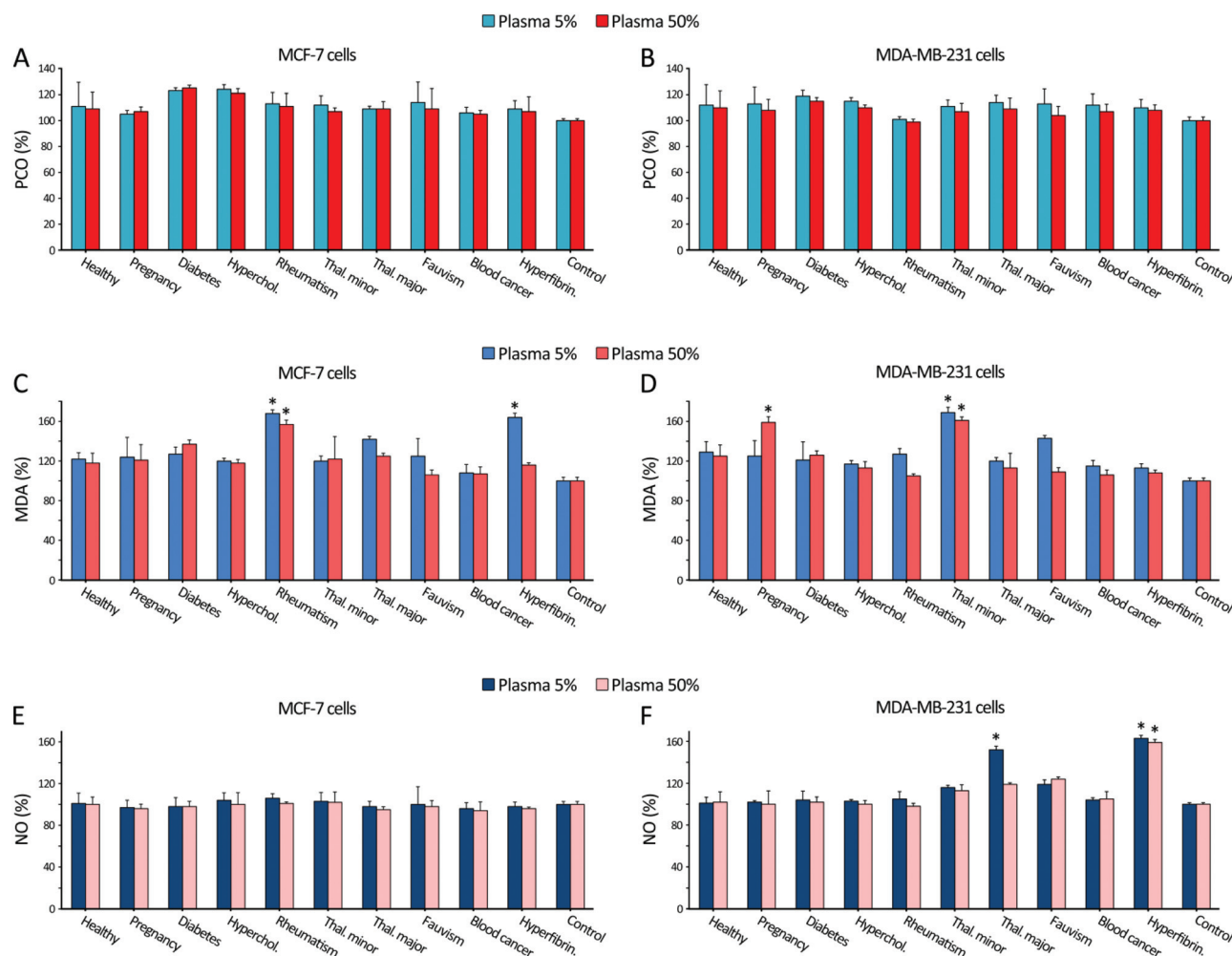
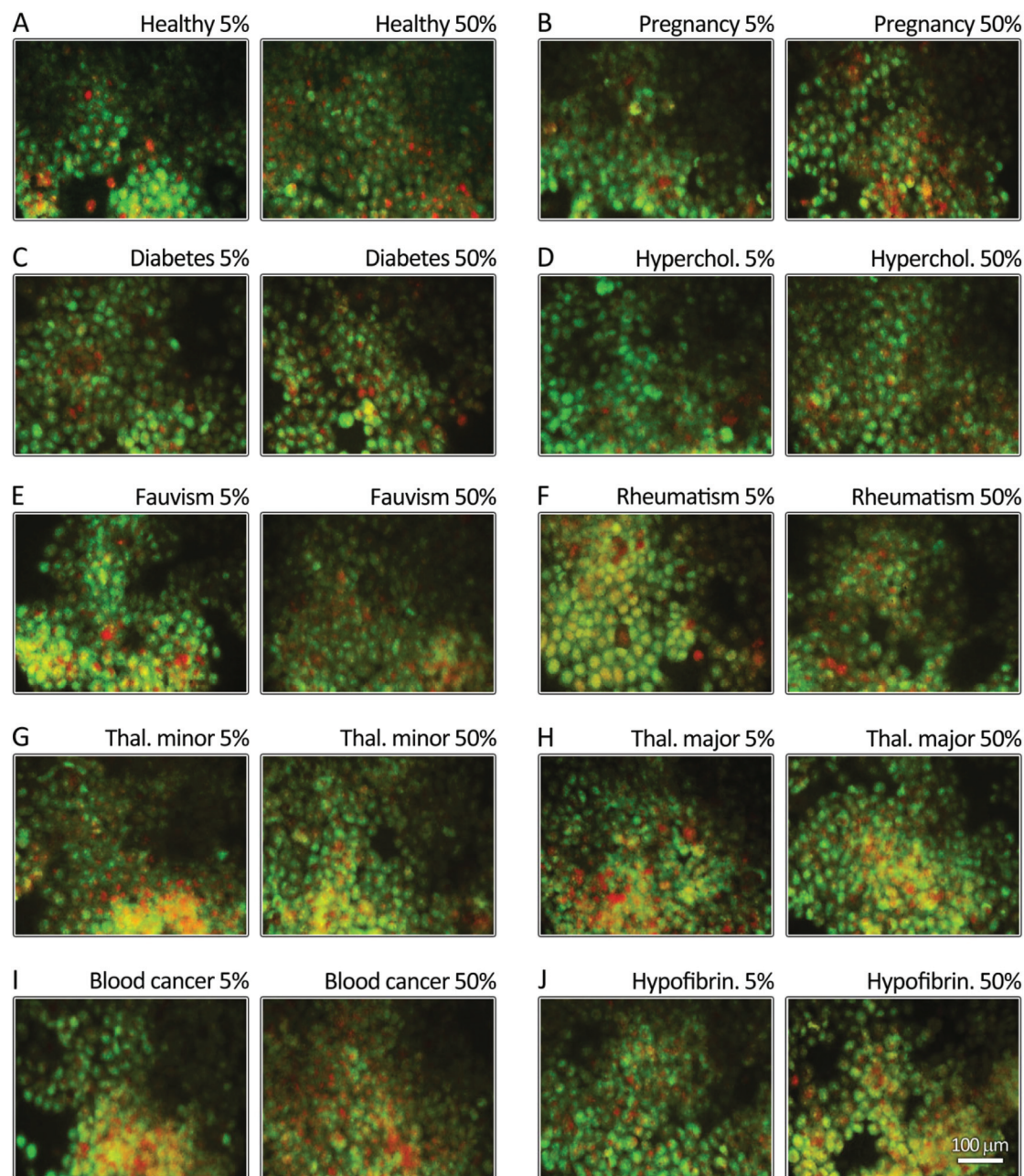


Fig. 5 Levels of (A and B) protein carbonylation, (C and D) MDA production, and (E and F) nitric oxide production MCF-7 and MDA-MB-231 cells, respectively, incubated with CCGO ( $100 \mu\text{g ml}^{-1}$ ) from different patients for 24 hours. Star (\*) represents significant differences ( $P < 0.05$ ) compared to other patients.

nogenemia (5% and 50%) patients, while the MCF-7 cells showed no inflammation responses in the presence of various CCGO sheets. These results indicated that the CCGO sheets of the various patients induced different levels of inflammation response depending on the protein composition/content of the corona and the cell type.

**3.3.4. Effects of the CCGO sheets on cell apoptosis and necrosis.** Double staining was performed for apoptosis and necrosis using annexin-V and propidium iodide (PI). Annexin-V can specifically bind externalized phosphatidylserine (PS),

which translocates from the inner surface of the plasma membrane to the outer surface, to provide an index of early apoptosis. Double staining of the cells is used as an efficient approach for differentiating the early apoptotic cells (annexin V+, green) from the late apoptotic/necrotic cells (annexin V+ and PI+, yellow/green-red). The cells were incubated with the CCGO sheets of the patients and were stained with the annexin-V and PI dyes. The apoptotic (green) and necrotic (yellow/green-red) cells were counted using fluorescence microscopy. The live cells did not appear in the images



**Fig. 6** Double staining of MCF-7 cells incubated with CCGO ( $100 \mu\text{g ml}^{-1}$ ) from different patients for 24 hours using PI (nuclei, green) and annexin-V (membrane, yellow to red). Green and yellow show the early apoptotic/necrotic cells. Green and red show the late apoptotic/necrotic cells.

**Table 3** Percentage of apoptotic and necrotic MCF-7 cells counted following incubation with CCGO (100  $\mu\text{g ml}^{-1}$ ) of various patients for 24 hours

CCGO sheets obtained from disease (5% and 50% plasma)	Early apoptotic cells (%) (MCF-7)	Late apoptotic or necrotic cells (%) (MCF-7)
Healthy 5%	27 $\pm$ 2%	38 $\pm$ 10%
Healthy 50%	17 $\pm$ 6%	48 $\pm$ 4%
Pregnancy 5%	23 $\pm$ 3%	36 $\pm$ 9%
Pregnancy 50%	20 $\pm$ 4%	47 $\pm$ 11%
Diabetes 5%	18 $\pm$ 4%	41 $\pm$ 8%
Diabetes 50%	14 $\pm$ 3%	49 $\pm$ 3%
Hypercholesterolemia 5%	29 $\pm$ 3%	33 $\pm$ 4%
Hypercholesterolemia 50%	16 $\pm$ 5%	44 $\pm$ 3%
Fauvism 5%	22 $\pm$ 7%	39 $\pm$ 7%
Fauvism 50%	18 $\pm$ 5%	48 $\pm$ 3%
Rheumatism 5%	25 $\pm$ 2%	34 $\pm$ 9%
Rheumatism 50%	17 $\pm$ 11%	46 $\pm$ 4%
Thalassemia minor 5%	19 $\pm$ 3%	44 $\pm$ 3%
Thalassemia minor 50%	23 $\pm$ 7%	35 $\pm$ 3%
Thalassemia major 5%	22 $\pm$ 5%	37 $\pm$ 5%
Thalassemia major 50%	17 $\pm$ 4%	46 $\pm$ 7%
Blood cancer 5%	18 $\pm$ 4%	42 $\pm$ 4%
Blood cancer 50%	13 $\pm$ 2%	56 $\pm$ 3%
Hypofibrinogenemia 5%	15 $\pm$ 3%	51 $\pm$ 3%
Hypofibrinogenemia 50%	21 $\pm$ 6%	47 $\pm$ 6%

because they were not stained. As shown in Fig. 6 and Table 3, the cells incubated with the CCGO sheets from different diseases exhibited significantly different apoptosis (green) and late apoptosis/necrosis (yellow/green-red) levels. For the MCF-7 cells, the CCGO sheets that were obtained from the healthy (5%), hypercholesterolemia (5%), and rheumatism (5%) plasmas mainly induced apoptosis, while the CCGO sheets from the blood cancer (50%), hypofibrinogenemia (5%), diabetes (50%) and fauvism (50%) plasmas predominantly resulted in necrosis. For the MDA-MB-231 cells, the CCGO sheets from the pregnancy (5%), hypercholesterolemia (5%), thalassemia major (5% and 50%) and blood cancer (50%) plasmas chiefly induced apoptosis, while the sheets from the pregnancy (50%), diabetes (5%), fauvism (50%), thalassemia minor (5%), and blood cancer (5%) plasmas resulted in necrosis (Fig. 7 and Table 4). Apoptosis in the cells incubated with CCGO sheets that exhibited cross-talk was potentially triggered by several mechanisms, including the direct interaction with the plasma membrane, generation of ROS, inactivation of the mitochondria, activation of different signaling pathways, and nanoparticle internalization. In contrast, necrosis mainly resulted from acute cellular damage.<sup>72–75</sup> Because the cell membrane integrity and signaling activation strongly depend on the cell–nanomaterial interactions, the varying apoptotic/necrotic effects of the CCGO sheets that were obtained from the different diseases may be attributed to their different interactions with the cells.

**3.3.5. Cellular uptake of the CCGO sheets.** Because the biological effects of nano-sized objects mainly depend on their cellular uptake, we evaluated the cellular uptake capacities of CCGO sheets that were obtained from various patients.<sup>76</sup> The

cellular uptake of the CCGO sheets from various patients was studied using a confocal microscope. For the MDA-MB-231 cell, the CCGO sheets from the blood cancer (5% and 50%), diabetes (5% and 50%), and hypercholesterolemia (5% and 50%) plasmas induced greater levels of lysosome formation relative to the hypofibrinogenemia plasma (Fig. 8). Remarkably, the internalization of the CCGO sheets that were obtained from the hypofibrinogenemia (5% and 50%) and hypercholesterolemia (5% and 50%) patients induced greater levels of lysosome formation in the MCF-7 cells relative to those obtained from the diabetic and blood cancer patients (Fig. 9). Due to the different protein compositions/contents of the corona, the CCGO sheets from various patients had different affinities for the plasma membrane and different adhesion strengths. In addition, several additional reports have confirmed the significant role of protein corona on the nanoparticle uptake level.<sup>77–80</sup>

The formation of the protein corona is known to reduce the adhesion strength of nanomaterials to the plasma membrane and decreases their internalization efficiency.<sup>81</sup> The cellular uptake of small and large CCGO sheets, which is an energy-dependent process,<sup>82</sup> occurs through clathrin-mediated endocytosis and phagocytosis respectively. Eventually, the internalized sheets are located in the lysosomes.<sup>77</sup> Therefore, the lysotracker assay is a suitable method for probing the intracellular concentrations and trafficking of the CCGO sheets because it detects the abundance of the lysosomes. By using this method, the nanomaterial does not need to be labeled, which could affect the protein corona decoration.

### 3.4. Hemolysis analysis

Because the intravenous and oral routes are the most common routes for administering nano-sized objects into live subjects, the compatibility of blood with the CCGO sheets from different patients is important. Thus, the CCGO sheets from different patients were incubated with red blood cells (RBCs) and the release of hemoglobin, which is a known result of cell lysis, was measured (Fig. 10A and B). The CCGO sheets from various patients exhibited different hemolysis effects. For example, the CCGO sheets from the diabetes (5%) and thalassemia minor (50%) patients exhibited the highest hemolytic activities, while that of the blood cancer (50%) patients showed the lowest hemolytic activity.

To determine whether hemolysis affects the formation of the protein corona, we evaluated the obtained CCGO sheets following incubation with the plasmas from normal and partially lysed blood samples (Fig. 10C). The protein patterns of the CCGO sheets that were obtained from the two conditions were significantly different. The protein bands marked by the yellow arrows only appeared in the hard corona of the normal blood samples. Therefore, the plasma alterations mediated by hemolysis influence the protein corona formation. It is possible that the autoimmune hemolytic anemia that occurred during the different diseases/conditions (*e.g.*, lymphoma, chronic lymphatic leukemia, rheumatoid arthritis, and infection) influenced the competitive binding of proteins on the

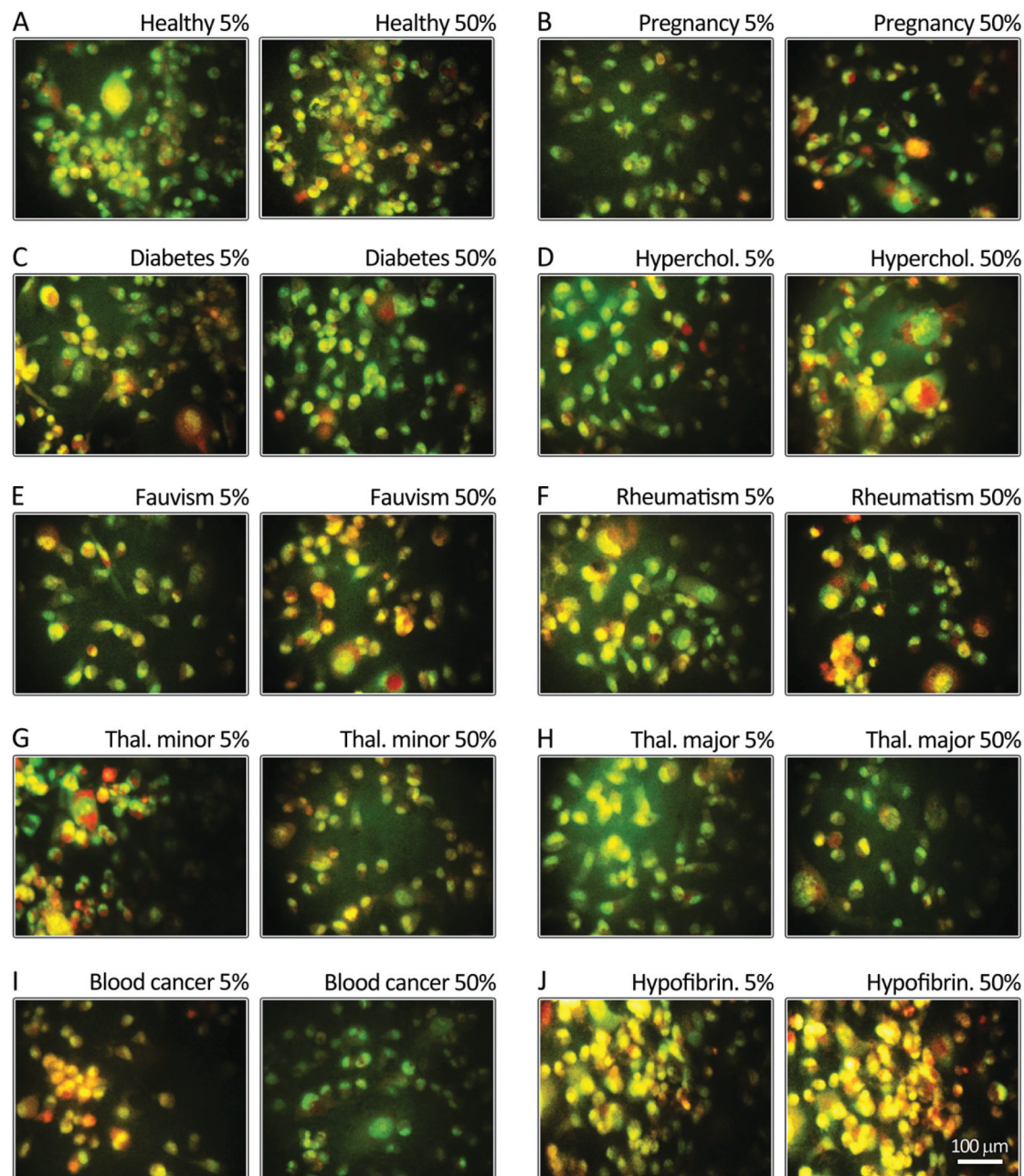


Fig. 7 Double staining of MDA-MB-231 cells incubated with CCGO ( $100 \mu\text{g ml}^{-1}$ ) from different patients for 24 hours using PI and annexin-V. Green and yellow/green-red show the early apoptotic and late apoptotic/necrotic cells respectively.

surfaces of the sheets. In conclusion, the hemolysis that occurs concurrently during the different diseases/conditions can change the plasma homeostasis and result in the formation of a personalized protein corona.

### 3.5. Circular dichroism (CD)

Far-ultraviolet CD spectroscopy was used to evaluate the secondary structural changes of fibrinogen and albumin proteins in the presence of increasing GO sheet concentrations (Fig. 11A and B). The CD spectrum of fibrinogen and albumin

showed two negative peaks at 208 and 220 nm, which indicated classic proteins containing  $\beta$ -sheet and  $\alpha$ -helix structures. The GO sheets altered the secondary structure of fibrinogen in a concentration dependent manner. Generally, as the GO concentrations increased, which corresponded to decreased ellipticity at 208 and 220 nm, the  $\alpha$ -helix content of the fibrinogen decreased significantly (Fig. 11A). In contrast, the addition of increasing GO sheet concentrations did not considerably affect the secondary structure of the albumin protein. As shown in Fig. 11B, the ellipticity at 208 and 220 nm

**Table 4** Percentage of apoptotic and necrotic MDA-MB-231 cells counted following incubation with CCGO ( $100 \mu\text{g ml}^{-1}$ ) of various patients for 24 hours

CCGO sheets obtained from disease (5% and 50% plasma)	Early apoptotic cells (%) (MDA-MB-231)	Late apoptotic or necrotic cells (%) (MDA-MB-231)
Healthy 5%	22 ± 9%	41 ± 6%
Healthy 50%	21 ± 6%	49 ± 8%
Pregnancy 5%	26 ± 3%	43 ± 5%
Pregnancy 50%	17 ± 2%	55 ± 3%
Diabetes 5%	19 ± 4%	51 ± 5%
Diabetes 50%	24 ± 7%	42 ± 3%
Hypercholesterolemia 5%	28 ± 2%	37 ± 4%
Hypercholesterolemia 50%	21 ± 8%	48 ± 7%
Fauvism 5%	19 ± 11%	41 ± 11%
Fauvism 50%	15 ± 3%	54 ± 4%
Rheumatism 5%	23 ± 5%	39 ± 5%
Rheumatism 50%	21 ± 9%	47 ± 13%
Thalassemia minor 5%	17 ± 3%	55 ± 3%
Thalassemia minor 50%	23 ± 9%	49 ± 9%
Thalassemia major 5%	27 ± 3%	41 ± 11%
Thalassemia major 50%	26 ± 4%	46 ± 6%
Blood cancer 5%	19 ± 6%	51 ± 2%
Blood cancer 50%	26 ± 3%	41 ± 5%
Hypofibrinogenemia 5%	22 ± 10%	49 ± 5%
Hypofibrinogenemia 50%	24 ± 4%	46 ± 7%

showed slight changes in the presence of increasing concentrations of GO sheets. Nanosheet-bound proteins may undergo structural changes that affect the formation of protein corona and its subsequent physiological responses.<sup>83</sup> Protein conformational changes that occur following their sorption onto the GO sheet surface could uncover buried/hydrophobic sequences that interact non-specifically with other proteins. Therefore, protein folding is an important parameter when considering the protein compositions/contents of corona. In contrast, unfolding of the fibrinogen protein, which occurred during adsorption on the NP surface, has been reported to trigger immune responses by activating the Mac-1 receptor and causing inflammation.<sup>61,62</sup> This finding suggests that NP-induced unfolding of proteins could be an important factor that governs the therapeutic/toxic impacts of nanomaterials and their physiological responses. Because different patients have personalized protein coronas, the plasma proteins (*e.g.*, albumin, fibrinogen, apolipoproteins, and complement factors) potentially have different accessibility to the nanomaterial surfaces in various patients. Therefore, the plasma proteins that are associated within the protein corona may have different conformations in various patients. In contrast,

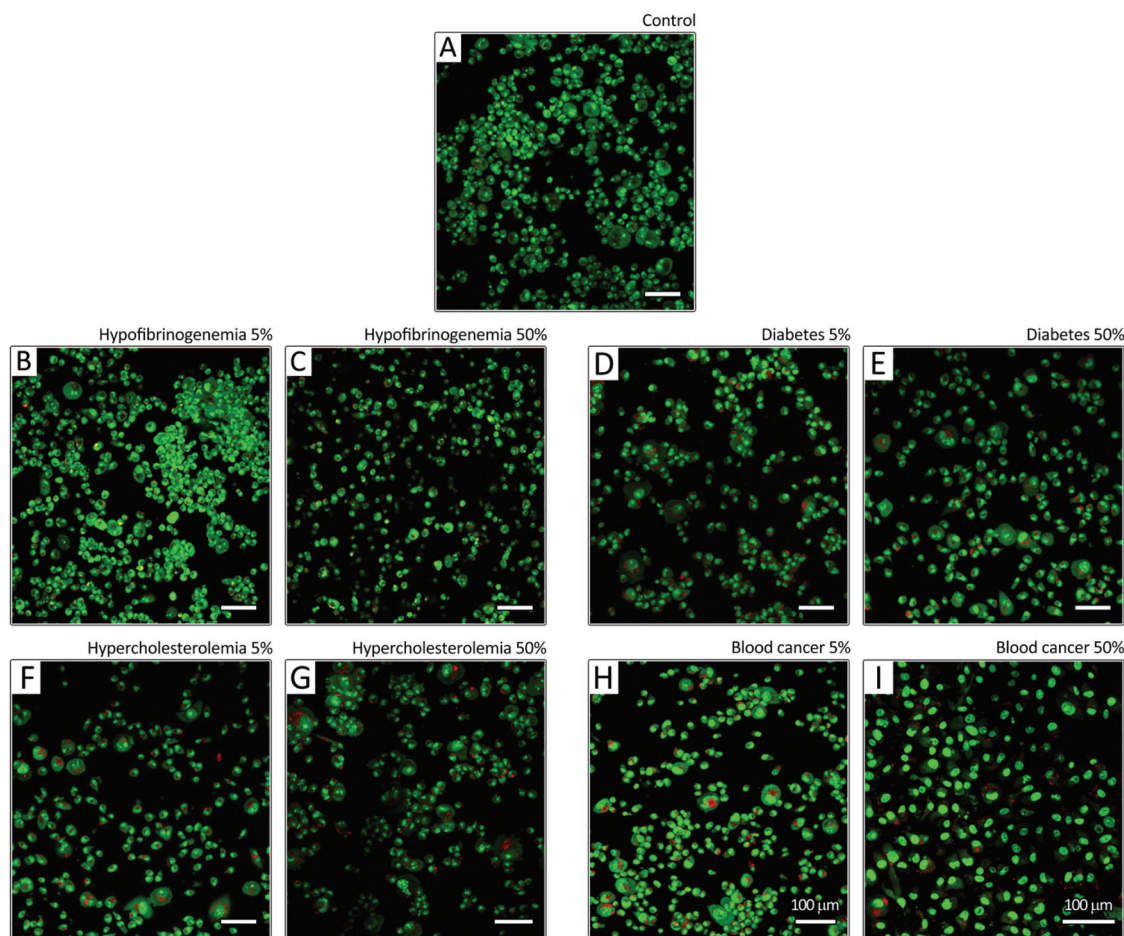


**Fig. 8** Lysosome induction in MDA-MB-231 cells treated with CCGO ( $100 \mu\text{g ml}^{-1}$ ) from different diseases (hypofibrinogenemia, hypercholesterolemia, diabetes, blood cancer). The lysosome and cell are seen as red and green fluorescence respectively.

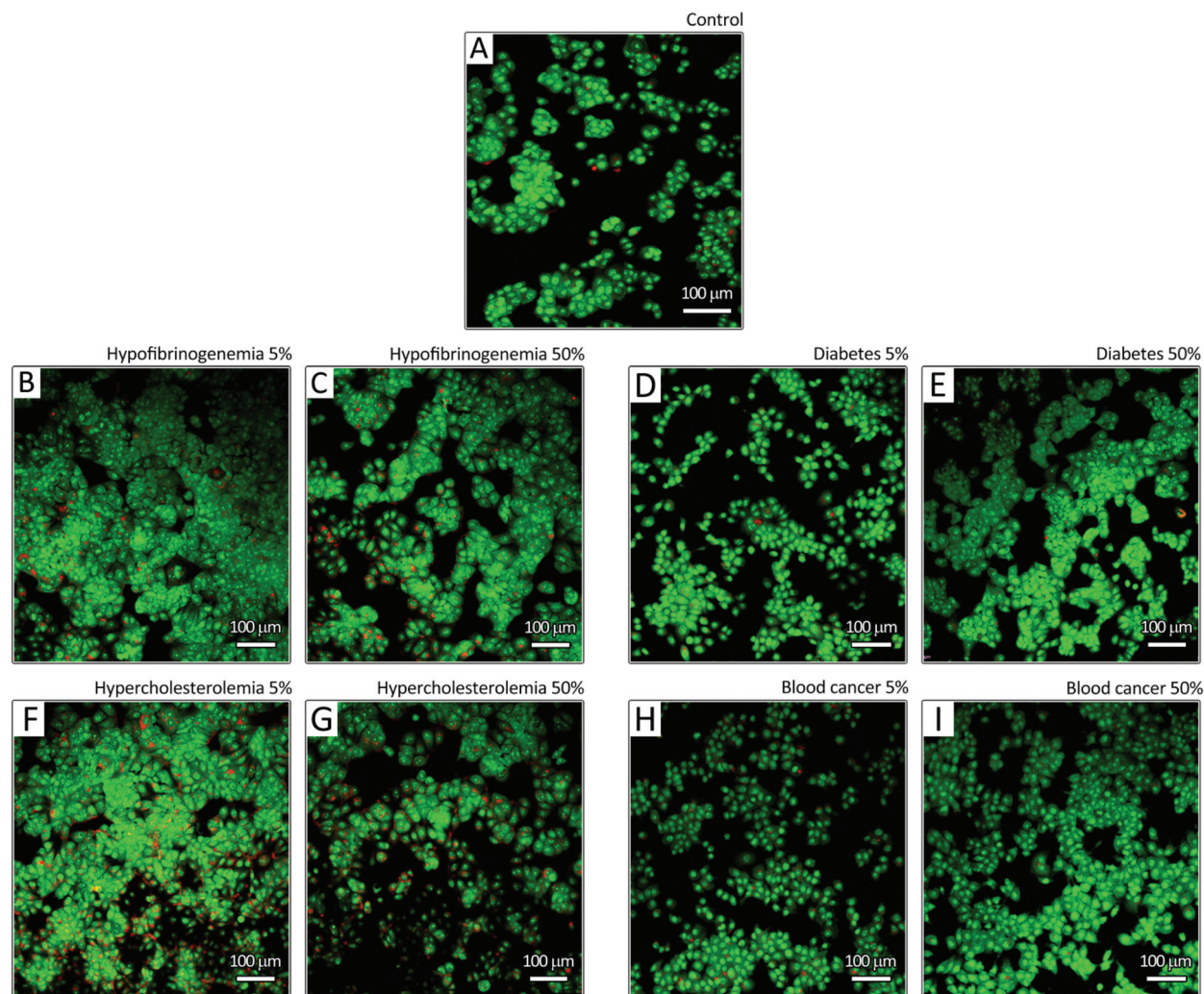


**Fig. 9** Lysosome induction in MCF-7 cells treated with CCGO ( $100 \mu\text{g ml}^{-1}$ ) from different diseases (hypofibrinogenemia, hypercholesterolemia, diabetes, blood cancer). The lysosome and cell are seen as red and green fluorescence respectively.

the protein changes that are mediated by disease may affect the binding affinities of the proteins toward the nanomaterial, the orientation of the proteins on the nanomaterial surface and the subsequent protein folding. For example, the albumin/protein glycosylation and fibrinogen deficiencies, which occurred in the diabetic and hypofibrinogenemia patients, respectively, can affect the adsorption and accessibility of these proteins to the nanomaterial surface. This finding agrees with the results of previous studies and shows that albumin modifications influence their binding to nanoparticles and the subsequent interactions of the nanoparticles with the cells.<sup>84</sup>

## 4. Conclusion

In this study, we investigated the effects of exposure to plasma obtained from individuals with various conditions on the formation and composition of protein coronas on GO sheets and

their biological outcomes. The differences in the plasmas of patients with various conditions (*i.e.*, hypofibrinogenemia, blood cancer, thalassemia major, thalassemia minor, rheumatism, favism, hypercholesterolemia, diabetes, and pregnancy) significantly affected the formation of the protein corona and the cellular responses of the corona-coated graphene oxide sheets. Due to their different protein composition and content, the personalized, disease-specific protein coronas exhibited significantly different cellular toxicity, apoptosis/necrosis and uptake, ROS production, lipid peroxidation and inflammation response. In spite of the current view, which accepts that the exact same NMs exert the same therapeutic/toxic impacts on different individual patients, we demonstrated that the exact same NMs can exhibit different therapeutic/toxic impacts on different patients. Therefore, it can be concluded that the data obtained from each patient cannot be generalized to others. These findings indicate that individual characteristics of each disease, which can alter the

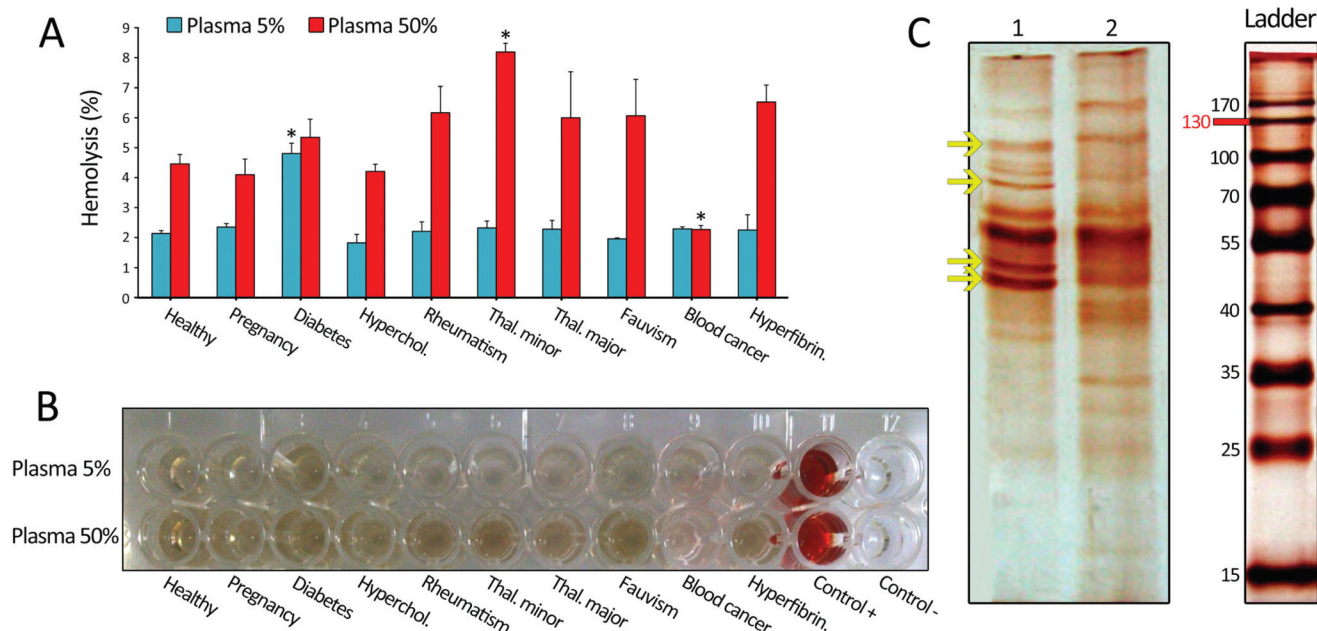


**Fig. 10** (A) Percentage of RBC hemolysis treated with CCGO ( $500 \mu\text{g ml}^{-1}$ ) from different patients for 180 minutes at  $37^\circ\text{C}$ ; star (\*) represents significant differences ( $P < 0.05$ ) compared to other patients. (B) Photographs of RBCs following incubation with CCGO ( $500 \mu\text{g ml}^{-1}$ ) from different patients for 180 minutes. (C) SDS-PAGE gel (15%) of CCGO obtained following incubation with plasmas (50%) of normal (1) and partially lysed (2) blood samples.

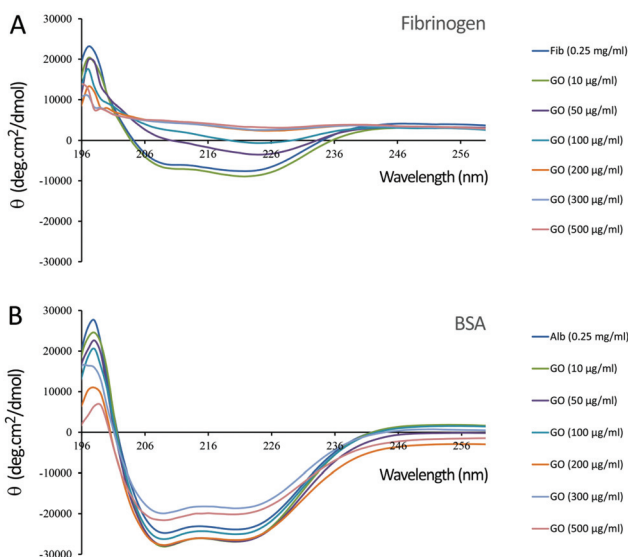


**Fig. 11** CD spectra of (A) fibrinogen and (B) BSA proteins in the presence and absence of GO.

plasma and subsequent protein corona, should be considered in the development of personalized nanomedicine. Therefore, by consideration of personalized protein corona, we can design patient-specific therapeutic NMs with maximal therapeutic efficacy and minimal side effects. In addition, these findings suggest that studies on the hard corona should be conducted using well-controlled human plasma to get a reliable under-

standing of the hard corona formation and its biological impacts.

## Acknowledgements

OA would like to thank the Research Council of Sharif University of Technology for supporting the work with Grant No. G930207.

## Notes and references

- 1 S. Krol, R. Macrez, F. Docagne, G. Defer, S. Laurent, M. Rahman, M. J. Hajipour, P. G. Kehoe and M. Mahmoudi, *Chem. Rev.*, 2012, **113**, 1877–1903.
- 2 M. J. Hajipour, K. M. Fromm, A. Akbar Ashkarran, D. Jimenez de Aberasturi, I. R. d. Larramendi, T. Rojo, V. Serpooshan, W. J. Parak and M. Mahmoudi, *Trends Biotechnol.*, 2012, **30**, 499–511.
- 3 W. C. Lee, C. H. Y. Lim, H. Shi, L. A. Tang, Y. Wang, C. T. Lim and K. P. Loh, *ACS Nano*, 2011, **5**, 7334–7341.
- 4 H. Mao, W. Chen, S. Laurent, C. Thirifays, C. Burtea, F. Rezaee and M. Mahmoudi, *Colloids Surf., B*, 2013, **109**, 212–218.
- 5 O. Akhavan, E. Ghaderi and M. Shahsavari, *Carbon*, 2013, **59**, 200–211.
- 6 O. Akhavan and E. Ghaderi, *Nanoscale*, 2013, **5**, 10316–10326.

- 7 O. Akhavan and E. Ghaderi, *J. Mater. Chem. B*, 2013, **1**, 6291–6301.
- 8 S. Y. Park, J. Park, S. H. Sim, M. G. Sung, K. S. Kim, B. H. Hong and S. Hong, *Adv. Mater.*, 2011, **23**, H263–H267.
- 9 O. Akhavan, *ACS Nano*, 2010, **4**, 4174–4180.
- 10 O. Akhavan and E. Ghaderi, *Small*, 2013, **9**, 3593–3601.
- 11 K. S. Novoselov, A. K. Geim, S. Morozov, D. Jiang, Y. Zhang, S. Dubonos, I. Grigorieva and A. Firsov, *Science*, 2004, **306**, 666–669.
- 12 W. Wei and X. Qu, *Small*, 2012, **8**, 2138–2151.
- 13 L. Feng, L. Wu and X. Qu, *Adv. Mater.*, 2013, **25**, 168–186.
- 14 K. Yang, S. Zhang, G. Zhang, X. Sun, S.-T. Lee and Z. Liu, *Nano Lett.*, 2010, **10**, 3318–3323.
- 15 O. Akhavan, A. Meidanchi, E. Ghaderi and S. Khoei, *J. Mater. Chem. B*, 2014, **2**, 3306–3314.
- 16 M. Abdollahad, A. Saeidi, M. Janmaleki, O. Mashinchian, M. Taghinejad, H. Taghinejad, S. Azimi, M. Mahmoudi and S. Mohajezadeh, *Nanoscale*, 2015, **7**, 1879–1887.
- 17 M. P. Monopoli, C. Åberg, A. Salvati and K. A. Dawson, *Nat. Nanotechnol.*, 2012, **7**, 779–786.
- 18 M. Mahmoudi, I. Lynch, M. R. Ejtehadi, M. P. Monopoli, F. B. Bombelli and S. Laurent, *Chem. Rev.*, 2011, **111**, 5610–5637.
- 19 G. Caracciolo, *Nanomedicine*, 2015, **11**, 543–557.
- 20 U. Sakulkhu, L. Maurizi, M. Mahmoudi, M. Motazacker, M. Vries, A. Gramoun, M.-G. O. Beuzelin, J.-P. Vallée, F. Rezaee and H. Hofmann, *Nanoscale*, 2014, **6**, 11439–11450.
- 21 C. D. Walkey and W. C. Chan, *Chem. Soc. Rev.*, 2012, **41**, 2780–2799.
- 22 M. Lundqvist, J. Stigler, T. Cedervall, T. Berggård, M. B. Flanagan, I. Lynch, G. Elia and K. Dawson, *ACS Nano*, 2011, **5**, 7503–7509.
- 23 D. Walczyk, F. B. Bombelli, M. P. Monopoli, I. Lynch and K. A. Dawson, *J. Am. Chem. Soc.*, 2010, **132**, 5761–5768.
- 24 P. Aggarwal, J. B. Hall, C. B. McLeland, M. A. Dobrovolskaia and S. E. McNeil, *Adv. Drug Delivery Rev.*, 2009, **61**, 428–437.
- 25 S. Laurent and M. Mahmoudi, *Int. J. Mol. Epidemiol. Genet.*, 2011, **2**, 367.
- 26 I. Lynch, T. Cedervall, M. Lundqvist, C. Cabaleiro-Lago, S. Linse and K. A. Dawson, *Adv. Colloid Interface Sci.*, 2007, **134**, 167–174.
- 27 M. J. Hajipour, O. Akhavan, A. Meidanchi, S. Laurent and M. Mahmoudi, *RSC Adv.*, 2014, **4**, 62557–62565.
- 28 M. J. Hajipour, S. Laurent, A. Aghaie, F. Rezaee and M. Mahmoudi, *Biomater. Sci.*, 2014, **2**, 1210–1221.
- 29 M. Mahmoudi, A. M. Abdelmonem, S. Behzadi, J. H. Clement, S. Dutz, M. R. Ejtehadi, R. Hartmann, K. Kantner, U. Linne and P. Maffre, *ACS Nano*, 2013, **7**, 6555–6562.
- 30 M. Mahmoudi, M. A. Shokrgozar and S. Behzadi, *Nanoscale*, 2013, **5**, 3240–3244.
- 31 S. Tenzer, D. Docter, J. Kuharev, A. Musyanovych, V. Fetz, R. Hecht, F. Schlenk, D. Fischer, K. Kiouptsi and C. Reinhardt, *Nat. Nanotechnol.*, 2013, **8**, 772–781.
- 32 M. P. Monopoli, D. Walczyk, A. Campbell, G. Elia, I. Lynch, F. Baldelli Bombelli and K. A. Dawson, *J. Am. Chem. Soc.*, 2011, **133**, 2525–2534.
- 33 M. Ghavami, S. Saffar, B. A. Emamy, A. Peirovi, M. A. Shokrgozar, V. Serpooshan and M. Mahmoudi, *RSC Adv.*, 2013, **3**, 1119–1126.
- 34 M. Mahmoudi, S. E. Lohse, C. J. Murphy, A. Fathizadeh, A. Montazeri and K. S. Suslick, *Nano Lett.*, 2013, **14**, 6–12.
- 35 S. Laurent, C. Burtea, C. Thirifays, F. Rezaee and M. Mahmoudi, *J. Colloid Interface Sci.*, 2013, **392**, 431–445.
- 36 M. Lundqvist, J. Stigler, G. Elia, I. Lynch, T. Cedervall and K. A. Dawson, *Proc. Natl. Acad. Sci. U. S. A.*, 2008, **105**, 14265–14270.
- 37 S. H. D. P. Lacerda, J. J. Park, C. Meuse, D. Pristiniski, M. L. Becker, A. Karim and J. F. Douglas, *ACS Nano*, 2009, **4**, 365–379.
- 38 U. Sakulkhu, M. Mahmoudi, L. Maurizi, J. Salaklang and H. Hofmann, *Sci. Rep.*, 2014, **4**.
- 39 G. Caracciolo, D. Pozzi, A. L. Capriotti, C. Cavaliere, S. Piovesana, H. Amenitsch and A. Laganà, *RSC Adv.*, 2015, **5**, 5967–5975.
- 40 G. Caracciolo, D. Caputo, D. Pozzi, V. Colapicchioni and R. Coppola, *Colloids Surf., B*, 2014, **123**, 673–678.
- 41 O. Akhavan and E. Ghaderi, *ACS Nano*, 2010, **4**, 5731–5736.
- 42 W. Hu, C. Peng, M. Lv, X. Li, Y. Zhang, N. Chen, C. Fan and Q. Huang, *ACS Nano*, 2011, **5**, 3693–3700.
- 43 A. Esfandiari, O. Akhavan and A. Irajizad, *J. Mater. Chem.*, 2011, **21**, 10907–10914.
- 44 T. Cedervall, I. Lynch, S. Lindman, T. Berggård, E. Thulin, H. Nilsson, K. A. Dawson and S. Linse, *Proc. Natl. Acad. Sci. U. S. A.*, 2007, **104**, 2050–2055.
- 45 H. Draper and M. Hadley, *Methods Enzymol.*, 1990, **186**, 421–431.
- 46 D. J. Stuehr, S. S. Gross, I. Sakuma, R. Levi and C. F. Nathan, *J. Exp. Med.*, 1989, **169**, 1011–1020.
- 47 A. Z. Reznick and L. Packer, *Methods Enzymol.*, 1994, **233**, 357–363.
- 48 H. C. Schniepp, J.-L. Li, M. J. McAllister, H. Sai, M. Herrera-Alonso, D. H. Adamson, R. K. Prud'homme, R. Car, D. A. Saville and I. A. Aksay, *J. Phys. Chem. B*, 2006, **110**, 8535–8539.
- 49 M. J. McAllister, J.-L. Li, D. H. Adamson, H. C. Schniepp, A. A. Abdala, J. Liu, M. Herrera-Alonso, D. L. Milius, R. Car and R. K. Prud'homme, *Chem. Mater.*, 2007, **19**, 4396–4404.
- 50 O. Akhavan, *Carbon*, 2010, **48**, 509–519.
- 51 O. Akhavan, M. Kalaei, Z. Alavi, S. Ghiasi and A. Esfandiari, *Carbon*, 2012, **50**, 3015–3025.
- 52 F. Liu and T. S. Seo, *Adv. Funct. Mater.*, 2010, **20**, 1930–1936.
- 53 A. Ferrari and J. Robertson, *Phys. Rev. B: Condens. Matter*, 2000, **61**, 14095.
- 54 S. Stankovich, D. A. Dikin, R. D. Piner, K. A. Kohlhaas, A. Kleinhammes, Y. Jia, Y. Wu, S. T. Nguyen and R. S. Ruoff, *Carbon*, 2007, **45**, 1558–1565.

- 55 A. Ferrari, J. Meyer, V. Scardaci, C. Casiraghi, M. Lazzeri, F. Mauri, S. Piscanec, D. Jiang, K. Novoselov and S. Roth, *Phys. Rev. Lett.*, 2006, **97**, 187401.
- 56 L. Malard, M. Pimenta, G. Dresselhaus and M. Dresselhaus, *Phys. Rep.*, 2009, **473**, 51–87.
- 57 D. Graf, F. Molitor, K. Ensslin, C. Stampfer, A. Jungen, C. Hierold and L. Wirtz, *Nano Lett.*, 2007, **7**, 238–242.
- 58 K. S. Kim, Y. Zhao, H. Jang, S. Y. Lee, J. M. Kim, K. S. Kim, J.-H. Ahn, P. Kim, J.-Y. Choi and B. H. Hong, *Nature*, 2009, **457**, 706–710.
- 59 I. Calizo, A. Balandin, W. Bao, F. Miao and C. Lau, *Nano Lett.*, 2007, **7**, 2645–2649.
- 60 O. Parolini, F. Alviano, G. P. Bagnara, G. Bilic, H. J. Bühring, M. Evangelista, S. Hennerbichler, B. Liu, M. Magatti and N. Mao, *Stem Cells*, 2008, **26**, 300–311.
- 61 Z. J. Deng, M. Liang, M. Monteiro, I. Toth and R. F. Minchin, *Nat. Nanotechnol.*, 2011, **6**, 39–44.
- 62 Z. J. Deng, M. Liang, I. Toth, M. J. Monteiro and R. F. Minchin, *ACS Nano*, 2012, **6**, 8962–8969.
- 63 R. H. Burdon, *Free Radical Biol. Med.*, 1995, **18**, 775–794.
- 64 D. Kültz, *Annu. Rev. Physiol.*, 2005, **67**, 225–257.
- 65 L. Minai, D. Yeheskely-Hayon and D. Yelin, *Sci. Rep.*, 2013, **3**.
- 66 F. Jiang, Y. Zhang and G. J. Dusting, *Pharmacol. Rev.*, 2011, **63**, 218–242.
- 67 A. L. Edinger and C. B. Thompson, *Curr. Opin. Cell Biol.*, 2004, **16**, 663–669.
- 68 G. Huang, H. Chen, Y. Dong, X. Luo, H. Yu, Z. Moore, E. A. Bey, D. A. Boothman and J. Gao, *Theranostics*, 2013, **3**, 116.
- 69 A. Manke, L. Wang and Y. Rojanasakul, *BioMed Res. Int.*, 2013, 2013.
- 70 K. Ando and T. Fujita, *Free Radical Biol. Med.*, 2009, **47**, 213–218.
- 71 D. A. Wink, Y. Vodovotz, J. Laval, F. Laval, M. W. Dewhirst and J. B. Mitchell, *Carcinogenesis*, 1998, **19**, 711–721.
- 72 Y. Li, Y. Liu, Y. Fu, T. Wei, L. Le Guyader, G. Gao, R.-S. Liu, Y.-Z. Chang and C. Chen, *Biomaterials*, 2012, **33**, 402–411.
- 73 J. Rauch, W. Kolch, S. Laurent and M. Mahmoudi, *Chem. Rev.*, 2013, **113**, 3391–3406.
- 74 J. Rauch, W. Kolch and M. Mahmoudi, *Sci. Rep.*, 2012, **2**.
- 75 O. Akhavan, E. Ghaderi and A. Akhavan, *Biomaterials*, 2012, **33**, 8017–8025.
- 76 T. Lammel, P. Boisseaux, M.-L. Fernández-Cruz and J. M. Navas, *Part. Fibre Toxicol.*, 2013, **10**, 27.
- 77 Q. Mu, G. Su, L. Li, B. O. Gilbertson, L. H. Yu, Q. Zhang, Y.-P. Sun and B. Yan, *ACS Appl. Mater. Interfaces*, 2012, **4**, 2259–2266.
- 78 H. Herd, N. Daum, A. T. Jones, H. Huwer, H. Ghandehari and C.-M. Lehr, *ACS Nano*, 2013, **7**, 1961–1973.
- 79 E. C. Cho, Q. Zhang and Y. Xia, *Nat. Nanotechnol.*, 2011, **6**, 385–391.
- 80 L. Treuel, X. Jiang and G. U. Nienhaus, *J. R. Soc., Interface*, 2013, **10**, 20120939.
- 81 A. Lesniak, F. Fenaroli, M. P. Monopoli, C. Åberg, K. A. Dawson and A. Salvati, *ACS Nano*, 2012, **6**, 5845–5857.
- 82 J. Huang, C. Zong, H. Shen, M. Liu, B. Chen, B. Ren and Z. Zhang, *Small*, 2012, **8**, 2577–2584.
- 83 M. Mahmoudi, M. A. Shokrgozar, S. Sardari, M. K. Moghadam, H. Vali, S. Laurent and P. Stroeve, *Nanoscale*, 2011, **3**, 1127–1138.
- 84 L. Treuel, S. Brandholt, P. Maffre, S. Wiegele, L. Shang and G. U. Nienhaus, *ACS Nano*, 2013, **8**, 503–513.